Performance Evaluation of Surface Riding Wave Energy Converter with Linear Electric Generator

Chungkuk Jin*, HeonYong Kang, MooHyun Kim, Farid P. Bakti
Department of Ocean Engineering, Texas A&M University,
College Station, TX, USA
* Corresponding author: kenjin0519@gmail.com

Abstract

In this study, we devised a new WEC (wave energy converter) called SR-WEC (Surface Riding WEC). The SR-WEC consists of two bodies: the outer cylinder with an armature assembly (body #1) and a magnet assembly (body #2) sliding inside the armature. For the SR-WEC, the relative sliding displacement and velocity are caused by gravity acceleration and the outer cylinder's motions, and they lead to electrical power generation. To evaluate its performance, a numerical simulation tool was developed, which solves the fully-coupled floater-mooring-generator dynamics. During the developing stage, the appropriate hydrodynamics model, sliding mechanics model, mooring dynamics model, and LEG (linear electric generator) electro-magnetic model were independently developed and then fully coupled in time domain to account for the cross-coupling interactions among them. Then, the developed simulation tool was verified component by component against various laboratory tests. Subsequently, systematic parametric studies were conducted with several important design parameters under various wave conditions to enhance power generation. After that, the average output power was evaluated in enlarged operational wave conditions. The present SR-WEC is particularly designed to be efficient at low sea states, which is good since they cover the majority of typical annual sea states.

Keywords: Wave energy converter, surface riding, linear electric generator, mooring line, floater-mooring-generator interaction, time-domain simulation

1. Introduction

Renewable energy resources, such as wind, ocean wave, and solar energy, have been considered as an alternative and environmentally friendly option to replace conventional energy resources. They are expected to account for 47.7% of the total energy consumption in 2040 based on a global renewable energy scenario [1]. Among them, ocean waves are a promising energy resource because of its highest energy density (2-3 kW/m^2), continuous availability (up to 90% of the time), and minimal negative environmental impact [2]. The global gross resource of the ocean wave is estimated to be in a range of 1-10 TW [3, 4].

In this regard, various WECs (wave energy converters) have been proposed. Among many technical aspects, the proper selection of the PTO (power take-off) system is important in improving conversion efficiency. Hydraulic systems (e.g. Pelamis [5]), turbines (e.g. Wave Dragon [6]), and direct-drive WECs (e.g. PowerBuoy [7]) are popular PTO systems. Various types of WEC devices and their simulation methodologies were presented in Ref. [8]. The hydraulic PTO system requires additional energy conversion to operate the rotary generator, which makes a device complex. Additional energy losses are inevitable in the process of double energy conversion. Also, the complexity of the conversion process can lead to reliability and maintenance issues [9], especially in harsh ocean environments. On the other hand, direct-drive WECs with the LEG (linear electric generator) produce power from the relative translational motions between the permanent magnet and coiled armature. They do not require any intermediate step; thus, the design can be simpler [2].

In recent decades, a number of experiments and numerical studies have been performed on the direct-drive WECs. For example, Prudell et al. [10] devised a freely floating dual-buoy WEC and conducted a laboratory experiment to estimate its performance. Kim et al. [11] designed a dual-buoy WEC, which utilized three resonant motions of two bodies and moon-pool, and carried out a laboratory experiment under regular and random wave conditions. Their experimental results were also compared with the results of time-domain dynamics simulations under the random-wave excitation [12]. Lejerskog et al. [13] conducted large-scale sea tests of the point absorber that was mounted at the seabed of the Lysekil research site in Sweden. They concluded that higher output power can be achieved in upward motions than downward motions. Stelzer and Joshi [14] also studied a similar point absorber under random wave excitations using numerical simulations. Zheng et al. [15] designed the variable aperture point absorber for enhancing survivability, reducing cost, and improving wave power absorption. Linear and nonlinear hydrodynamic models were compared for the two-body WEC [16] and submerged point absorber [17]. In addition, various design-optimization strategies have been adopted to improve the performance of the direct-drive WEC. Parametric studies were performed to find the proper generator and structural design [18, 19]. Resonance of dual-body WECs was adjusted to maximize the relative motion by using linear springs connected between two bodies [20-22]. The tuned inertia mass was utilized in a point absorber to increase power absorption and broaden the effective wave frequency range [23]. Control systems, such as latching control [24] and model predictive control [25], were adopted to improve the overall output power.

In this study, we developed a hydro-dynamics/linear-generator fully coupled simulation program to investigate the performance of an innovative SR-WEC (Surface Riding WEC) devised by authors [26]. It mainly consists of an outer cylinder equipped with a coiled armature assembly and a magnet assembly sliding along a center rod (see Fig. 1). Compared to other direct-drive WECs that utilize relative heave motions, SR-WEC uses the sliding motion inside a surface-riding and pitching horizontal cylinder. It is hard to find similar concepts and relevant simulations in publicly available literature [27]. The SR-WEC is specially devised to generate appreciable electrical power even in low sea states, which typically cover 90 % of the annual sea state e.g. East Coast in the U.S. (31.887 N 74.921 W). It is possible since both wave heights and lengths are reduced in low sea states for wave slopes to remain about the same. SR-WEC generates the sliding motion by the gravity acceleration, while most existing LEG-based devices utilize inertial acceleration. Various optimization methods can be employed to enhance output power further.

To evaluate the SR-WEC's performance, the present time-domain simulation program was developed and used to solve the fully-coupled floater-mooring-generator interaction. Several major considerations and algorithms were made to develop the numerical model. First, the outer cylinder interacts with waves, and thus its hydrodynamic coefficients and wave-excitation force were estimated based on potential theory in frequency domain [28] and they were utilized in the subsequent time-domain motion-simulation program. Second, the sliding mechanism of the magnet assembly with time-varying contact and friction forces should be well understood and modeled. Third, a reasonable collision model was developed at both ends of the outer cylinder to assess the impact-induced velocity, load, and fatigue by the magnet assembly. Fourth, the PTO force between the coil on the outer cylinder and the sliding magnet assembly should be well estimated to correctly estimate the resisting force and generated power. Fifth, a single point mooring system is installed and connected to the outer cylinder for a station-keeping purpose, and the floater-mooring interaction should be solved. The numerical modeling of sliding mechanism and collision at both ends was validated through comparisons with the physical system after mounting and pitching the SR-WEC on harmonic actuators with the PTO off. The numerical generator dynamics was also verified through comparisons with the laboratory experiments of Prudell et al. [10] with PTO on. Afterward, a series of parametric studies were performed with the validated numerical model to better understand the system's sensitivity on the design parameters so that the results can be used as the improved design for given annual sea states.

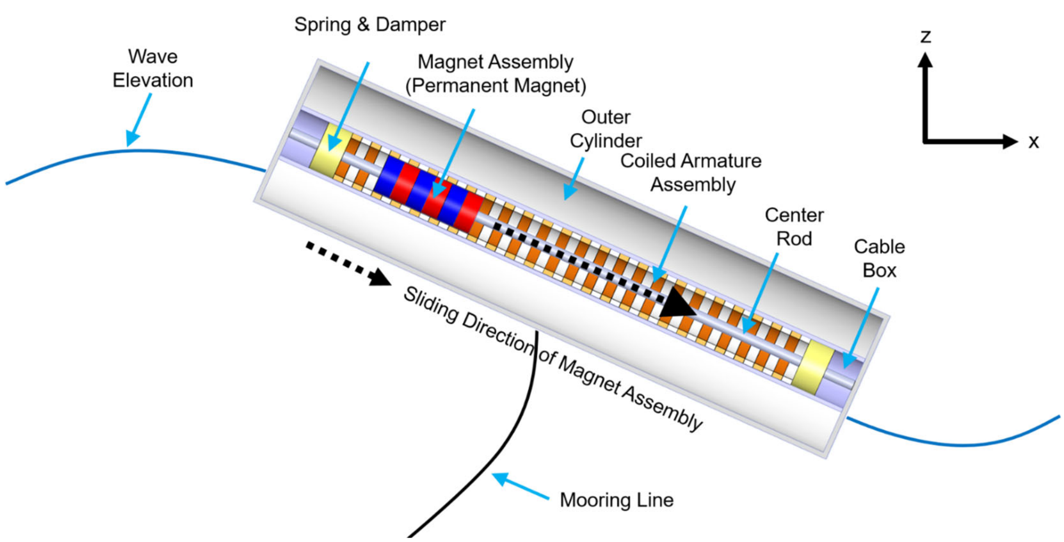

(a) Design

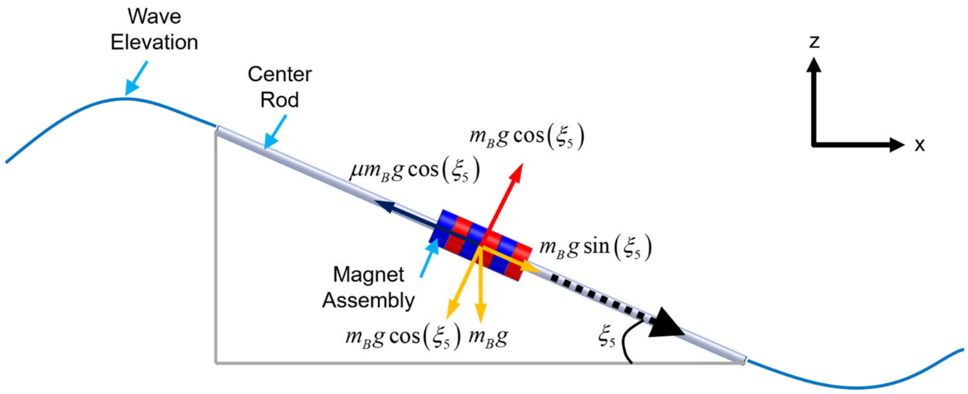

(b) Working principle

Fig. 1. Design and operation principle of the SR-WEC.

2. Design and Operation Principle

The design and operation principle of SR-WEC are presented in Fig. 1. The device mainly consists of the outer cylinder equipped with the armature assembly and the magnet assembly. The magnet assembly is composed of neodymium (NdFeB) magnets, supporting lamination steel, and linear ball bearings in detail. The linear ball bearings in the magnet assembly are in contact with a fixed center rod, which allows single-degree-of-freedom (SDOF) motion in the sliding direction along the center rod. The armature assembly, composed of coil and lamination steel, is installed to the outer cylinder and surrounds the magnet assembly. The outer cylinder interacts with the surrounding ocean fluid. The spring-damper system, which is referred to as the end damper, is located at both ends of the outer cylinder to alleviate collision damage from the magnet assembly. Ring masses are also located at both ends to provide a large mass moment of inertia about the y-axis (M_{55}) so that pitch natural frequency (1.65 rad/s) can be close to peak frequency in low sea states. As shown in Fig. 2, a single point mooring line is connected to the bottom center of the outer cylinder for position keeping, and cylinder's longitudinal direction is parallel to the dominant wave direction. Table 1 summarizes important design parameters.

Electric power is generated by relative motions between the magnet and armature assemblies. As shown in Fig. 1(b), the relative motion by sliding is mainly induced by the pitch motion of the outer cylinder. As the inclination angle is larger than the minimum sliding angle, the magnet assembly starts to slide by gravity. The detailed formulations are given in Section 3.

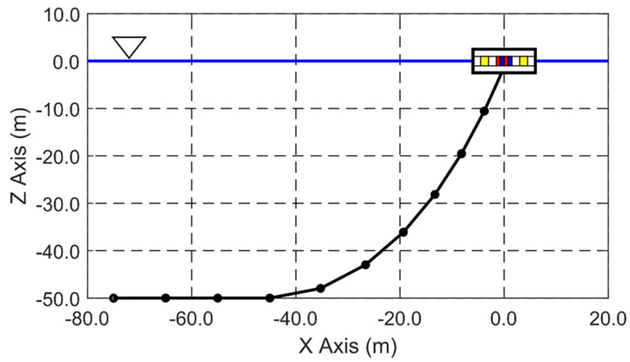

Fig. 2. Side view of SR-WEC with a mooring line.

Table 1. Important parameters of SR-WEC.

Component	Item	Value	Unit
Outer cylinder	Length	8	m
	Diameter	2.6	m
	Mass	21368	kg
Magnet assembly	Length	1	m
	Diameter	0.38	m
	Mass	400	kg
	Air gap	0.5	cm
Linear electric generator	Phase resistance	4.58	Ω
	Phase inductance	190	mH
	Magnet pole pitch	72	mm
	Coil pitch	72	mm
Mooring line (Studlink Chain)	Nominal diameter	1.5	cm
	Length	100	m
	Mass/unit length	4.9	kg/m
	Minimum breaking load	263.9	kN
Mass matrix of SR-WEC	M_{11}, M_{22}, M_{33}	21768	kg
	M_{44}	18343	$kg \cdot m^2$
	M_{55}, M_{66}	273508	$kg \cdot m^2$

3. Coupled Time-Domain Simulation

A hydrodynamics-mechanics-generator fully-coupled time-domain simulation program was developed to assess the performance of the SR-WEC i.e. floater-mooring-generator interactions were solved at each time step to evaluate their dynamic responses, mooring tension, and electric output power. The time-domain dynamic analysis allows non-linear loads to be considered. Section 3 explains the theory and formulations of the time-domain simulation and coupling methods among the floater (i.e. outer cylinder), magnet assembly, and mooring line.

3.1. Floating-Body Model

In time domain, the 6 DOF dynamic responses of the outer cylinder can be evaluated by solving the Cummins equation [29] as:

$$
\begin{aligned}
&\left(M_{ij} + A_{ij}^{\infty}\right)\ddot{\xi}_j\left(t\right) + B_{ij}^{E}\dot{\xi}_j\left(t\right) + K_{ij}\xi_j\left(t\right) \\
&= F_i^{W}\left(t\right) + F_i^{C}\left(t\right) + F_i^{M}\left(t\right) + F_i^{G}\left(t\right) + F_i^{S}\left(t\right) \quad i, j = 1, 2, ..., 6
\end{aligned}
\tag{1}
$$

where M_{ij} is the mass matrix, A_{ij}^{∞} is the added mass matrix at the infinite frequency, B_{ij}^{E} is the external damping matrix, K_{ij} is the system's stiffness matrix induced by hydrostatic and gravitational stiffness, $\xi_j = [\xi_1, \xi_2, \xi_3, \xi_4, \xi_5, \xi_6]^T$ is the displacement vector, i.e., surge, sway, heave, roll, pitch, and yaw, F_i^{W}, F_i^{C}, and F_i^{M} are, respectively, the first-order wave-excitation, convolution, and Morison drag force vectors, F_i^{G} is the PTO force vector induced by the interaction between the magnet and armature assemblies, and F_i^{S} is the spring force vector to couple the outer cylinder with the mooring line. The upper dot in the equations represents the time derivative of a variable.

Based on the assumption of linearity, A_{ij}^{∞}, F_i^{C}, and F_i^{W} can be obtained from the equivalent relationship between the impulse-response-function-based equations in time domain and the diffraction/radiation-based equations in frequency domain as follows:

$$A_{ij}^{\infty} = A_{ij}\left(\omega\right) + \int_0^{\infty} R_{ij}\left(t\right)\frac{\sin\left(\omega t\right)}{\omega}dt \tag{2}$$

$$F_i^{C}\left(t\right) = -\int_0^{\infty} R_{ij}\left(\tau\right)\dot{\xi}_j\left(t-\tau\right)d\tau \tag{3}$$

$$R_{ij}\left(t\right) = \frac{2}{\pi}\int_0^{\infty} B_{ij}\left(\omega\right)\cos\left(\omega t\right)d\omega \tag{4}$$

$$F_i^{W}\left(t\right) = \mathrm{Re}\left(\sum_{j=1}^{N} A_j^{1} L_i\left(\omega_j\right)e^{i\left(k_j x - \omega_j t - \alpha_j\right)}\right) \tag{5}$$

where R_{ij} is the retardation function, A_{ij} and B_{ij} are the added mass and the radiation damping as a function of angular frequency ω, and A_j^{1}, L_i, k_j, and α_j are wave amplitude, the linear transfer function, wavenumber, and random-phase angle, respectively. Frequency-dependent A_{ij}, B_{ij}, and L_i were obtained by a 3D diffraction/radiation program [28].

The Morison equation is widely used for the estimation of wave forces on slender bodies at its instantaneous position, which is composed of the linear inertia and non-linear drag terms [30]. The Morison equation is recommended for the wave-force evaluation of slender structures when the ratio of outer diameter D to wavelength λ_w is less than 0.2 ($D/\lambda_w = 0.12$ at natural period=3.81 sec) [31]. Since the inertia term was obtained from the diffraction/radiation potential theory, only the non-linear drag term was added for the viscous-drag-force evaluation. The Morison drag force per unit length for the moving cylindrical body can be written as:

$$F_i^M(t) = \frac{1}{2}\rho C_D D\left(u_i^n - \dot{\xi}_i^n\right)\left|u_i^n - \dot{\xi}_i^n\right| \tag{6}$$

where ρ is the density of water, C_D is the drag coefficient, and u_i is the surrounding fluid's velocity. Superscript n is the normal direction of a variable.

For SR-WEC, the mass of the magnet assembly was designed to be much lighter (1.9%) than that of the outer cylinder. In this regard, we evaluated the dynamic responses of the outer cylinder based on the total mass of the SR-WEC including the mass of the magnet assembly, instead of solving the two-body fully-coupled interaction between the outer cylinder and the magnet assembly.

3.2. Mooring-Line Model and Coupling with Floating Body

As mentioned before, a single-point mooring line was employed to maintain SR-WEC's original position. Therefore, the outer cylinder's motions are to be coupled with the mooring dynamics. Two governing equations were established to estimate the mooring dynamics and tension based on a rod theory [32], in which generalized coordinate was used and twisting motions and moments were neglected. Fig. 3 presents the rod theory's coordinate system. The generalized coordinate system is along the line, and thus the geometric nonlinearity can be automatically considered [33]. In the generalized coordinate system, $r_i(s,t)$ represents the position vector in 3D, which is a function of arc length s and time t to define space curve, r_i' denotes the unit tangent vector to the space curve, while r_i'' and $r_i' \times r_i''$ are the principal normal and bi-normal vectors, respectively. The prime in the equations denotes the spatial derivative of a variable.

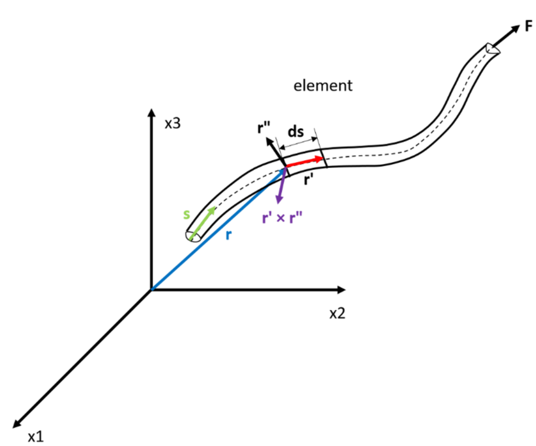

Fig. 3. Rod theory's coordinate system [34].

The equation of motion with the line's tension and bending effects can be described as follows:

$$-\left(EI r_i''\right)'' + \left(\tilde{\lambda} r_i'\right)' + q_i^D = m_D \ddot{r}_i \qquad i = 1,2,3 \tag{7}$$

where E is Young's modulus, I is the second moment of cross-sectional area, $\tilde{\lambda} = \tilde{T} - EI\kappa^2$ with effective tension $\tilde{T}$ and local curvature κ, while q_i^D and m_D are the distributed force vector and mass per unit length. In this case, q_i^D is the sum of wet weight vector per unit length $\tilde{w}_i^R$ ($= w_i^R + B_i^R$ where w_i^R and B_i^R are weight and buoyancy per unit length) and the wave force vector per unit length F_i^D. According to the Morison equation, F_i^D for the cylindrical body can be written as:

$$F_i^D = -C_A \rho A_E \ddot{r}_i^n + C_M \rho A_E \dot{u}_i^n + \frac{1}{2} C_D \rho D \left(u_i^n - \dot{r}_i^n\right)\left|u_i^n - \dot{r}_i^n\right| \tag{8}$$

where C_A and C_M are, respectively, the added mass and inertia coefficients, A_E is the external cross-sectional area. With $\tilde{w}_i^R$ and F_i^D, Eq. (7) can be rewritten as:

$$m_D \ddot{r}_i + C_A \rho A_E \ddot{r}_i^n + \left(EI r_i''\right)'' - \left(\tilde{\lambda} r_i'\right)' = \tilde{w}_i^R + C_M \rho A_E \dot{u}_i^n + \frac{1}{2} C_D \rho D \left(u_i^n - \dot{r}_i^n\right)\left|u_i^n - \dot{r}_i^n\right| \tag{9}$$

The mooring tension can separately be estimated by the extensible condition. Assuming linear and small extension, the mooring tension can be estimated by the following relationship:

$$r_i' \cdot r_i' = \left(1 + \frac{T}{EA_T}\right) \approx 1 + 2\frac{T}{EA_T} \approx 1 + 2\frac{\lambda}{EA_T} \tag{10}$$

where $A_T = A_E - A_I$ with the internal cross-sectional area A_I , T is the tension, and $\lambda (= T - EI\kappa^2)$ is the Lagrange multiplier. The equation of motion and extensible condition in Eqs. (9) and (10) are, therefore, governing equations for mooring-line analysis. Finally, Finite Element (FE) formulations of the governing equations were further derived by using the Galerkin method, which is detailed by Refs. [34, 35]. In the FE method, nonlinear behaviors can be captured by dividing a line into multiple high-order elements.

A mooring line was coupled with the outer cylinder through translational and rotational springs, which is a practical approach to connect several objects conveniently. The interaction force is delivered to the outer cylinder as spring force, and equal and opposite force is also transmitted to the top of the mooring line. Assuming the hinged connection, zero rotational stiffness was implemented. The spring force vector transmitted from the mooring line to the floating body can be expressed as [36]:

$$F_i^S = \tilde{K}_{ij}\left(\tilde{T}_{jk}\tilde{u}_k^R - \tilde{u}_j^C\right) \tag{11}$$

where $\tilde{K}_{ij}$ represents the coupling stiffness matrix, $\tilde{T}_{jk}$ denotes the transformation matrix between the floater's origin and the connection position, while $\tilde{u}_k^R$ and $\tilde{u}_j^C$ are, respectively, the displacement vectors of the rigid body and connection position.

3.3. Linear Generator Model

LEG was modeled to couple the two bodies and generate electric power. In the proposed design, the coiled armature assembly is attached to the outer cylinder whereas the magnet assembly freely slides along the center rod. The relative velocity between the armature and magnet assemblies induces the EMF (electromotive force), whose unit is voltage. According to Faraday's law of induction, the induced EMF E_b proportionally increases with a change in flux linkage $\lambda_{fl}(=N_c\phi_m)$ and can be calculated as [37]:

$$E_b = \frac{d\lambda_{fl}}{dt} = \frac{d\xi_7}{dt}\frac{d\lambda_{fl}}{d\xi_7} = \dot{\xi}_7\frac{d\lambda_{fl}}{d\xi_7} \tag{12}$$

where N_c is the number of turns, ϕ_m is magnetic flux, and ξ_7 is the displacement of the magnet assembly relative to the armature assembly. The EMF is proportional to the relative velocity.
Based on the RL (Resistor-Inductor) circuit, the following relationship can be used to compute the induced current [37]:

$$E_b = \left(R_L + R_C\right)\cdot i_c + L_P\frac{di_c}{dt} \tag{13}$$

where R_L and R_C are load and phase resistances, respectively, i_c is the induced electric current, and L_P is the phase inductance. The first-order ODE (ordinary differential equation) should be solved to acquire the induced current, and the fourth-order Runge-Kutta method was used.

After calculating the induced current, the PTO force can be estimated by using the Lorentz-force equation. The electrons of electric current experience the magnetic force under the given magnetic field, which can be regarded as an interaction force between the two bodies. The PTO force on the coiled armature assembly in the sliding direction can be written as:

$$F^{Gn} = i_c\oint d\mathbf{l}\times\mathbf{B}_m = -B_m l_c i_c \tag{14}$$

where B_m $(= B_f \cos(\pi\xi_7 / \tau)$ with the magnitude of magnetic flux density B_f and pole pitch τ) is the magnetic flux density, and l_c is the length of the coil that receives influences by the magnetic field at each time. According to Newton's third law, the equal and opposite force also acts on the magnet assembly. Since it acts in the sliding direction, at each time step, the PTO force was decomposed to calculate F_i^G for the outer cylinder. In general, B_f can be evaluated from electro-magnetic-filed simulation; however, in this study, a parametric study was conducted to find the proper B_f. In the parametric study, $B_f l_c$ is defined as the magnitude of EMF (or PTO force). Finally, the generated electric output power can be expressed as:

$$P_o = i_c^{\,2} R_L = i_c V_o \tag{15}$$

where V_o is the output voltage.

3.4. Magnet-Assembly Dynamics

Relative-displacement-based SDOF equation of motion for magnet assembly in sliding direction along the center rod can be written as:

$$m_B \ddot{\xi}_7(t) = F^L(t) - F^{Gn}(t) \tag{16}$$

where m_B is the mass of the magnet assembly and F^L is the sliding force.

The working principle of the magnet assembly was previously described (Fig. 1b). As the inclination angle of the outer cylinder ξ_5 (i.e. pitch motion) is higher than the minimum sliding angle associated with the given friction coefficient and lubrication condition, the magnet assembly starts to slide by gravity along the center rod.

The SDOF was defined in the body-fixed coordinate system located to the center of gravity of the outer cylinder. Since the coordinate center of the magnet assembly continuously moves at each time step due to the dynamic motions of the outer cylinder, the non-inertia reference frame, i.e., the accelerated coordinate system, was introduced to always keep the magnet assembly's coordinate center with respect to the center of gravity of the outer cylinder. The SDOF motion is, therefore, that of the magnet assembly relative to the body-fixed coordinate system of the outer cylinder in the sliding direction. In this coordinate system, the inertial forces, which are also known as the fictitious forces, should be added as external force terms. The inertial force is the production of the mass of the magnet assembly and acceleration of the outer cylinder. Considering the head wave condition, sway motion is generally small; thus, inertia force from sway motion was neglected. Therefore, F^L, which includes inertial forces, can be formulated as:

$$F^L(t) = m_B\left(g\sin\xi_5 + \ddot{\xi}_3\sin\xi_5 - \ddot{\xi}_1\cos\xi_5\right) - \operatorname{sgn}\left(\dot{\xi}_7\right)\mu m_B\left(g\cos\xi_5 + \ddot{\xi}_3\cos\xi_5 + \ddot{\xi}_1\sin\xi_5\right) \tag{17}$$

where g is gravity acceleration and μ is friction coefficient.

The equation of motion given in Eq. (17) does not account for the contact mechanism between two bodies at both ends of the outer cylinder. To realize the contact mechanism at both ends of the outer cylinder, conservation of momentum with the partial elastic condition was used. Then, the displacement and velocity of the magnet assembly in the sliding direction after a collision can be evaluated. The conservation of momentum and the coefficient of restitution can be expressed as:

$$m_a v_a(t_n) + m_b v_b(t_n) = m_a v_a(t_{n+1}) + m_b v_b(t_{n+1}) \tag{18}$$

$$R_E = \frac{v_b(t_{n+1}) - v_a(t_{n+1})}{v_a(t_n) - v_b(t_n)} \tag{19}$$

where v_a and v_b are the velocities of the objects #1 and #2, m_a and m_b are the masses of object #1 and #2, and R_E is the coefficient of restitution. By combining Eqs. (18) and (19), the velocity of object #1 after the collision can be derived as

$$v_a(t_{n+1}) = \frac{m_a v_a(t_n) + m_b v_b(t_n) + m_b R_E\left[v_b(t_n) - v_a(t_n)\right]}{m_a + m_b} \tag{20}$$

For SR-WEC, the mass of the outer cylinder is designed to be much larger than that of the magnet assembly; therefore, the terms related to the mass of the magnet assembly in Eq. (20) can be neglected. Moreover, for the same reason, the contribution of a collision to the outer cylinder's motion is assumed to be small, and the velocity of the outer cylinder is not influenced by the collision. Also, the non-inertia reference frame keeps the velocity of the outer cylinder zero from the view of the magnet assembly. Based on the above considerations, Eq. (20) can be simplified with the current variables of SR-WEC as:

$$\dot{\xi}_7(t_{n+1}) = -R_E\dot{\xi}_7(t_n) \tag{21}$$

When the magnet assembly does not contact both ends, Eq. (16) was used to solve the dynamic equation of motion. After the contact, Eq. (21) gave the instantaneous displacement and velocity of the magnet assembly.

3.5. Procedure of Time-Domain Simulation

Fig. 4 presents a flowchart describing the procedure of the present fully-coupled floater-mooring-generator time-domain simulation. First, the frequency-domain hydrodynamic computation was completed to obtain the frequency-dependent hydrodynamic coefficients and forces for the outer cylinder. Also, the initial parameters of the two bodies (outer cylinder and magnet assembly), mooring line, and generator were entered. Second, the retardation function and the added mass at infinite frequency were calculated. Third, at each time step, forces on two bodies and a mooring line were evaluated, which includes the wave, PTO, spring, and sliding forces. Fourth, the coupled equations of motion were solved by the Adams-Moulton implicit method combined with the Adams-Bashforth explicit method, in which iteration within a time step is not needed. The third and fourth steps were repeated until the last time step.

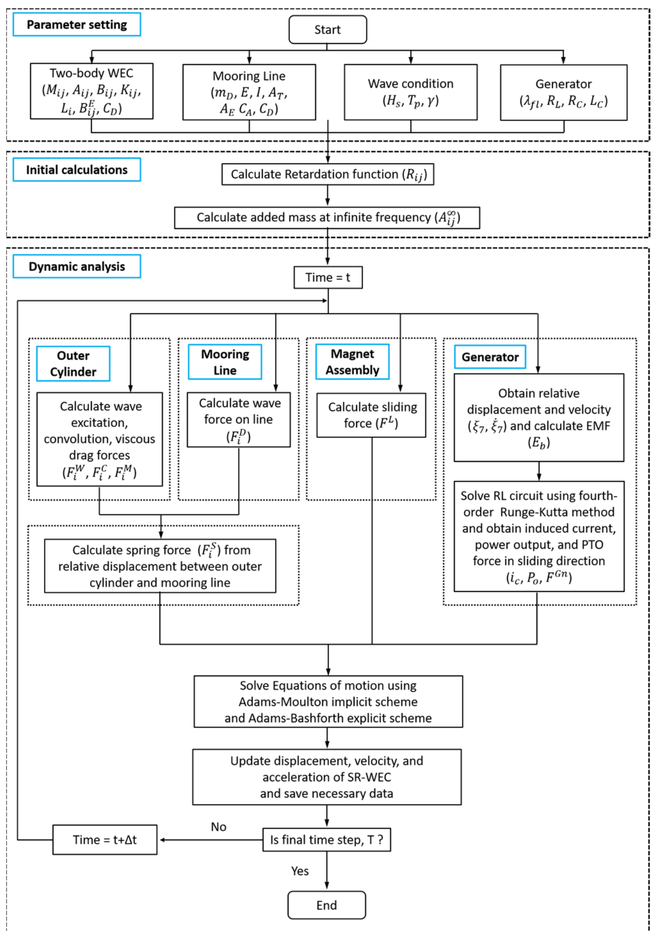

Fig. 4. Flowchart describing the time-domain simulation.

4. Validation of Numerical Model

Two comparative studies between the numerical simulation and experiment were carried out to validate the proposed simulation program: (i) the sliding mechanism of the magnet assembly without the LEG was confirmed by comparing the numerical simulations with the heave-pitch coupled actuator tests conducted by authors, and (ii) LEG dynamics by the present numerical simulation at different sea states was validated against laboratory tests conducted by Prudell et al. [10].

4.1. Validation of Sliding Mechanism

Fig. 5 shows the test setup of the heave-pitch coupled actuator test. Table 2 presents the dimension and mass of cylinders. An acrylic hollow tube was used for inner and outer cylinders while a center rod was made of stainless steel. A linear ball bearing (SSU20 by Thomson) was mounted to an inside of the inner cylinder to maximize the sliding performance with a low friction coefficient. At both ends of the outer cylinder, Styrofoam dampers were located to mitigate the impact force. There were two actuators (A-LST series by Zaber Technology) vertically installed at both ends of the outer cylinder so that the heave-pitch coupled motion of the outer cylinder can be emulated. As the outer cylinder moves with the actuators, the inner cylinder slides along the center rod. For this test, LEG was not installed since the main objective of the test was to check the sliding mechanism.

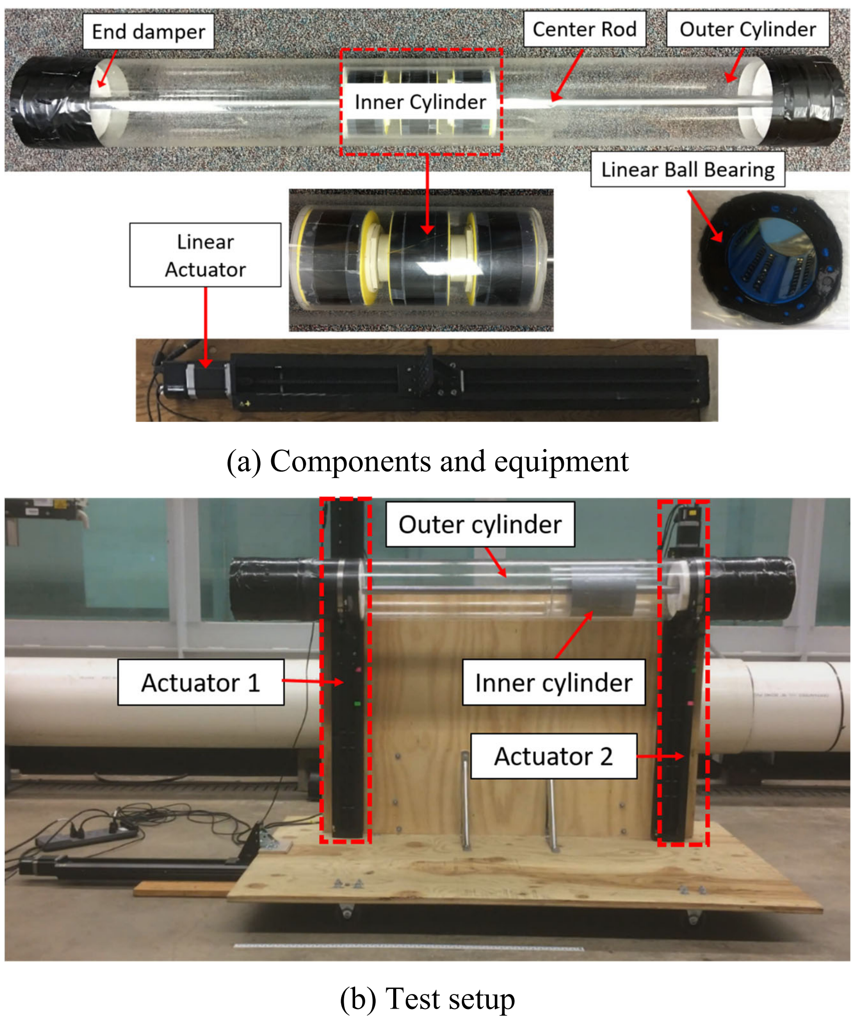

Fig. 5. Test setup of heave-pitch coupled actuator tests.

Table 2. Scaled WEC's mass and dimension.

Item		Value
Outer cylinder	Length	1.52 m
	Mass	9.51 kg
Inner cylinder	Length	0.3 m
	Mass	2.1 kg
Center rod	Outer diameter	0.025 m

First, the minimum sliding angle of the inner cylinder was checked. The inclination angle was increased from 0.2 degrees with an interval of 0.05 degrees, which results in the observed minimum sliding angle of around 0.5 degrees. The corresponding static friction coefficient was estimated from the minimum sliding angle.

Second, the dynamic friction coefficient along the sliding and collision mechanism at the ends were identified at different inclination angles. Fig. 6 shows the displacements of the inner cylinder in the sliding direction at inclination angles of 2 and 3 degrees. The dynamic friction coefficient is generally smaller than the static friction coefficient, and the identified dynamic friction coefficient is 75 % of the static friction coefficient to match the experimental results before a collision occurs. Also, the coefficient of restitution was checked by comparing the transient response after the collision. As shown in Fig. 6, the coefficient of restitution in the range of 0.36 ~ 0.39 best matches against the experiments. Those values were used in the ensuing simulation of SR-WEC.

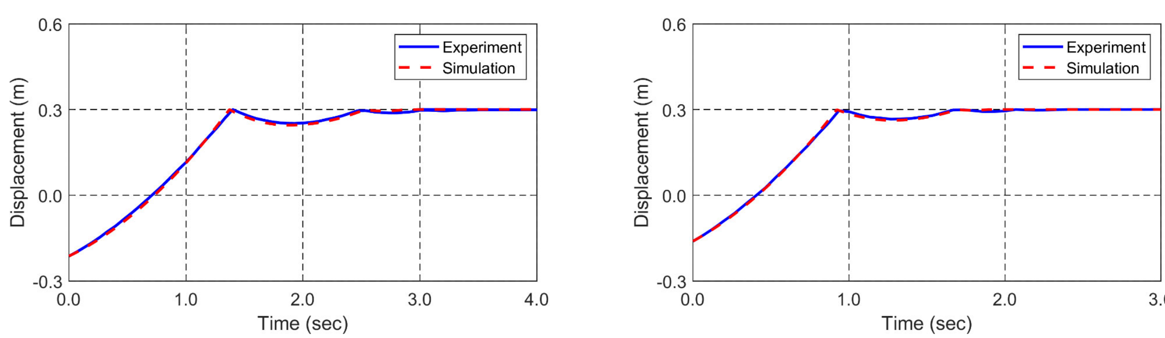

(a) (b)

Fig. 6. Time-history comparison of the displacement of the inner cylinder in the sliding direction at the inclination angles of 2 (a) and 3 (b) degrees.

Third, a heave-pitch coupled actuator test was performed, and the experimental results were compared with our simulation results. Fig. 7 shows the measured time-histories of the outer cylinder's pitch and heave motions, and the corresponding displacements and velocities of the inner cylinder are presented in Fig. 8. The same condition was also inputted in the numerical simulation. As shown in Fig. 8, with the coefficient of restitution of 0.38, the simulated magnitudes and trends of displacement and velocity coincide well against experimental values. Those well-matched sliding responses with the experiments, where the collision and those two coupled motions were involved, validate the formulation of the SR-WEC mechanics as explained in the previous section.

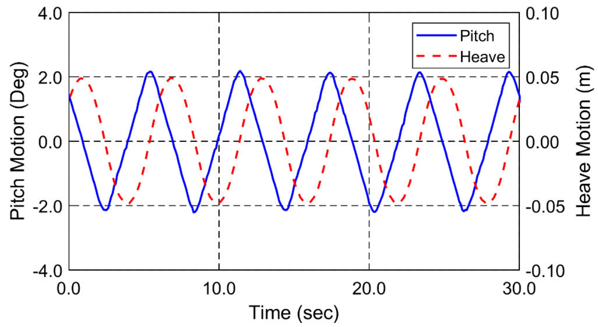

Fig. 7. Time-history of measured pitch and heave motions.

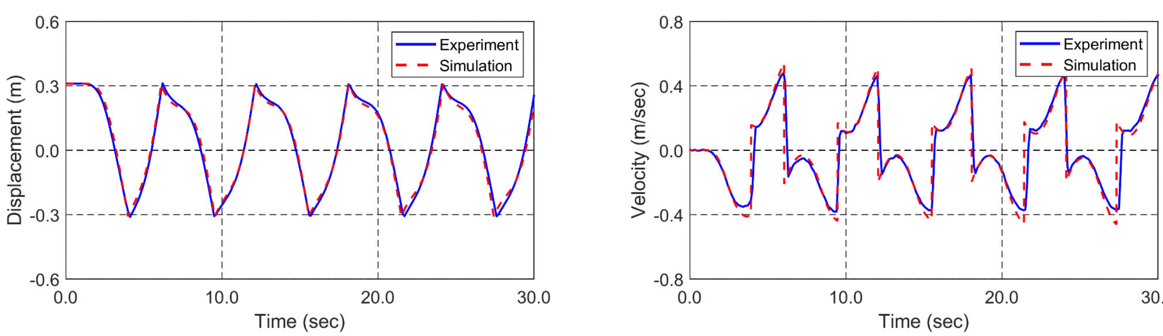

(a) (b)

Fig. 8. Time-history comparison of displacement (a) and velocity (b) of the inner cylinder in the sliding direction for the heave-pitch coupled actuator tests.

4.2. Validation of Generator Dynamics

The developed LEG simulation model was validated with the experimental data given in Prudell et al. [10]. The present formulations related to generator dynamics were confirmed through this validation. In the experiment, two-body heave-type WEC with LEG was tested in the laboratory. Armature and magnet assemblies were installed at inner and outer buoys, respectively. 960 NdFeB magnets were used to construct magnet assembly, and the three-phase Y connection was designed. The major LEG parameters are summarized in Table 3. Considering that the LEG performance only depends on the relative displacement and velocity, the difference in WEC type is irrelevant as long as those two inputs are the same.

Table 3. Major parameters for calculation of electric output power [10].

Parameter	Value	Units
Number of magnetic poles	4	-
Magnetic flux density	0.9037	T
Average circumference of the winding	1.81	m
Number of turns per slot	77	-
Reduction factor due to armature reaction	0.904	-
EMF magnitude at unit velocity	455.43	V
Phase resistance	4.58	Ω
Phase inductance	0.19	H
Wire diameter	1.628	mm

In their laboratory test, the dynamics of two floating bodies in waves was actually not considered. Instead, they assumed that the inner buoy is stationary while the outer buoy moves with wave elevation. Under this scenario, the heave-motion time series of the outer buoy is the same as wave-elevation time series while the inner buoy is fixed. Therefore, they actually utilized the measured time-histories of wave elevation as the relative heave motion between the two buoys. Then, they recorded the measured output power from the physical LEG for 900 sec for 8 different sea states. In the present numerical simulation, authors also generated the wave-elevation time histories for 900 sec for the same sea states and used them as the input relative displacement of the same numerical LEG. The wave-elevation time series were generated by superposing 100 regular waves from the PM (Pierson-Moskowitz) spectrum.

Fig. 9 shows the time-history examples of wave elevation, the EMF, the induced current, and input and output powers obtained by our numerical simulation in the case of significant wave height H_S=0.44 m, zero-crossing period T_Z =6.4 sec, and load resistance R_L=3.9 Ω. The time histories are presented for the first 100 seconds. The LEG-related frequencies are higher than those of wave elevation. In other words, the generator dynamics solver requires smaller time steps than the floating-body dynamics solver. The 120-degree phase difference of the three-phase system was also confirmed in the time histories. As summarized in Table 4, the calculated average output powers are well-matched with those from experiments i.e. their maximum difference is only 5.2 %. The results in Table 4 demonstrate that the developed numerical LEG solver can be utilized for the ensuing SR-WEC simulations.

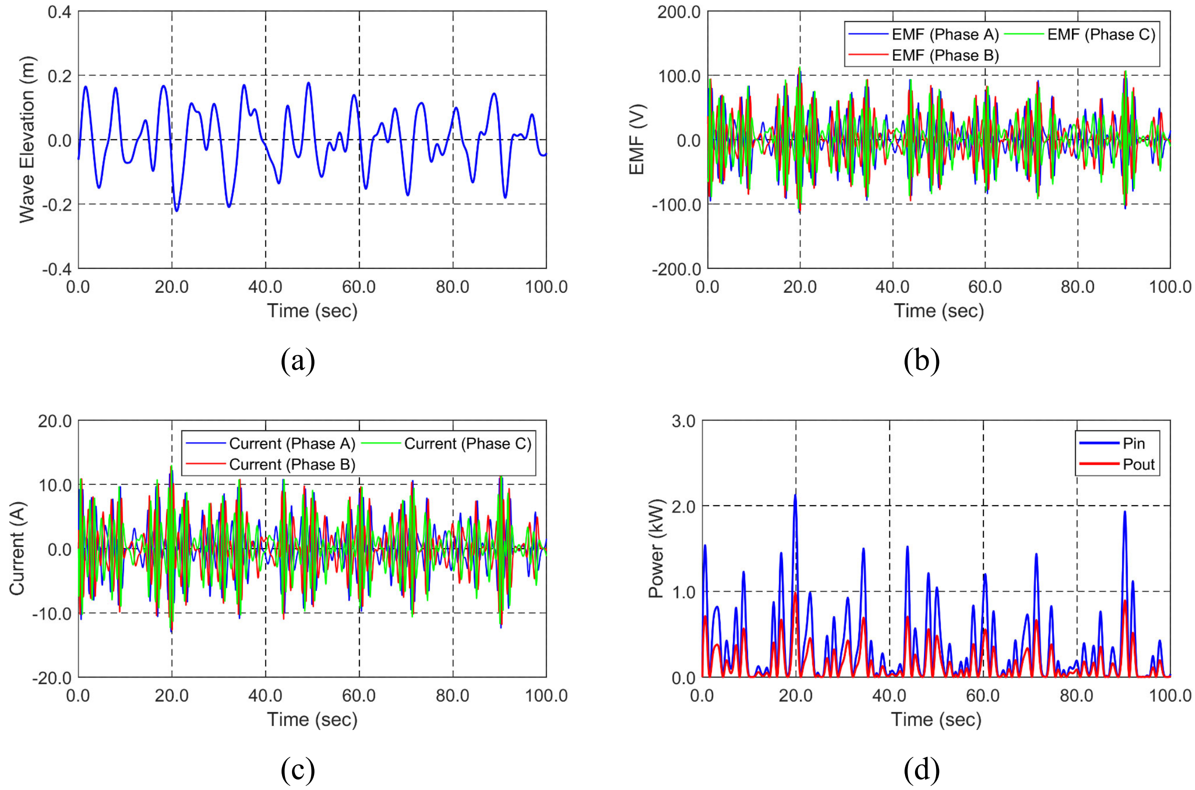

Fig. 9. Time histories of wave elevation (a), EMF (b), induced current (c), and input and output powers (d) for significant wave height of 0.44 m, zero-crossing period of 6.4 sec, and load resistance of 3.9 Ω.

Table 4. Comparison of average output power between numerical and physical LEGs in various sea conditions [10].

Sea condition	H_S (m)	T_Z (sec)	R_L (Ω)	Average output power (kW)		Percentage difference (%)
				Experiment	Simulation	
1	0.44	6.4	3.9	0.177	0.179	1.1
2	0.64	6.2	4.1	0.368	0.387	5.0
3	1.02	7.6	4.3	0.669	0.658	1.7
4	1.25	7.6	4.4	0.920	0.917	0.3
5	1.52	7.6	4.7	1.237	1.224	1.1
6	2.03	7.6	5.2	1.758	1.734	1.4
7	2.54	7.6	5.8	2.207	2.141	3.0
8	3.04	7.6	6.4	2.587	2.455	5.2

5. Results and Discussions

5.1. Frequency-Domain Simulation

The frequency-domain simulation was firstly conducted to compute the hydrodynamic coefficients and forces on the outer cylinder. A 3D diffraction/radiation program, WAMIT [28], was used to estimate the frequency-dependent added mass, the radiation damping coefficient, and the first-order wave-excitation force. These outputs were utilized in the time-domain simulation. SR-WEC is half-submerged, and the submerged surface panels were modeled, as shown in Fig. 10. 30 wave frequencies were selected from 0.1 rad/s to 5.0 rad/s, and the wave direction was parallel to the longitudinal direction of SR-WEC. The mass matrix is based on the entire SR-WEC (See Table 1), including the magnet assembly located at the center of gravity of SR-WEC.

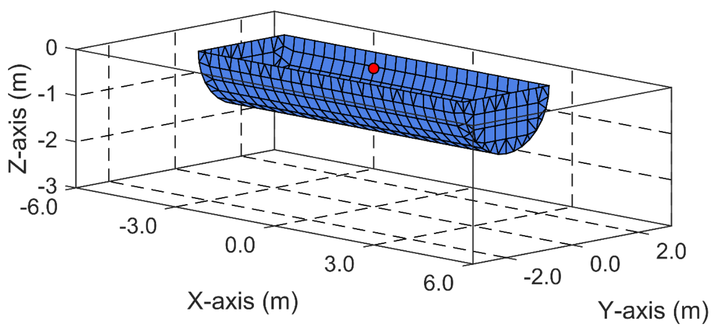

Fig. 10. Panel model of the wet surface of the outer cylinder with 468 panels.

Fig. 11 shows the resulting surge, heave, and pitch Response Amplitude Operators (RAOs). After convergence test with different panel numbers as in the previous study [38], the converged results are given in Fig.11. The pitch natural frequency is 1.65 rad/s (3.81 sec), and thus excellent sliding performance is expected at low sea states. The computed added masses and radiation damping coefficients for the 3-DOF motions are plotted in Fig. 12.

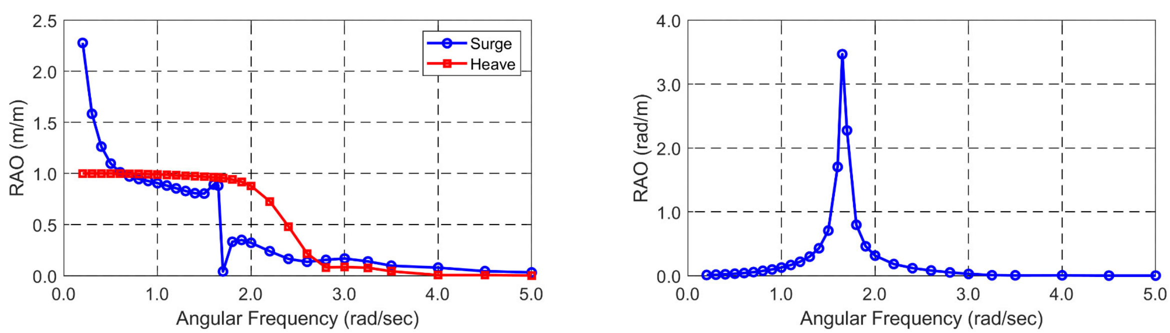

(a) Surge and heave RAOs

(b) Pitch RAO

Fig. 11. Surge, heave (a), and pitch (b) RAOs from 3D diffraction/radiation program.

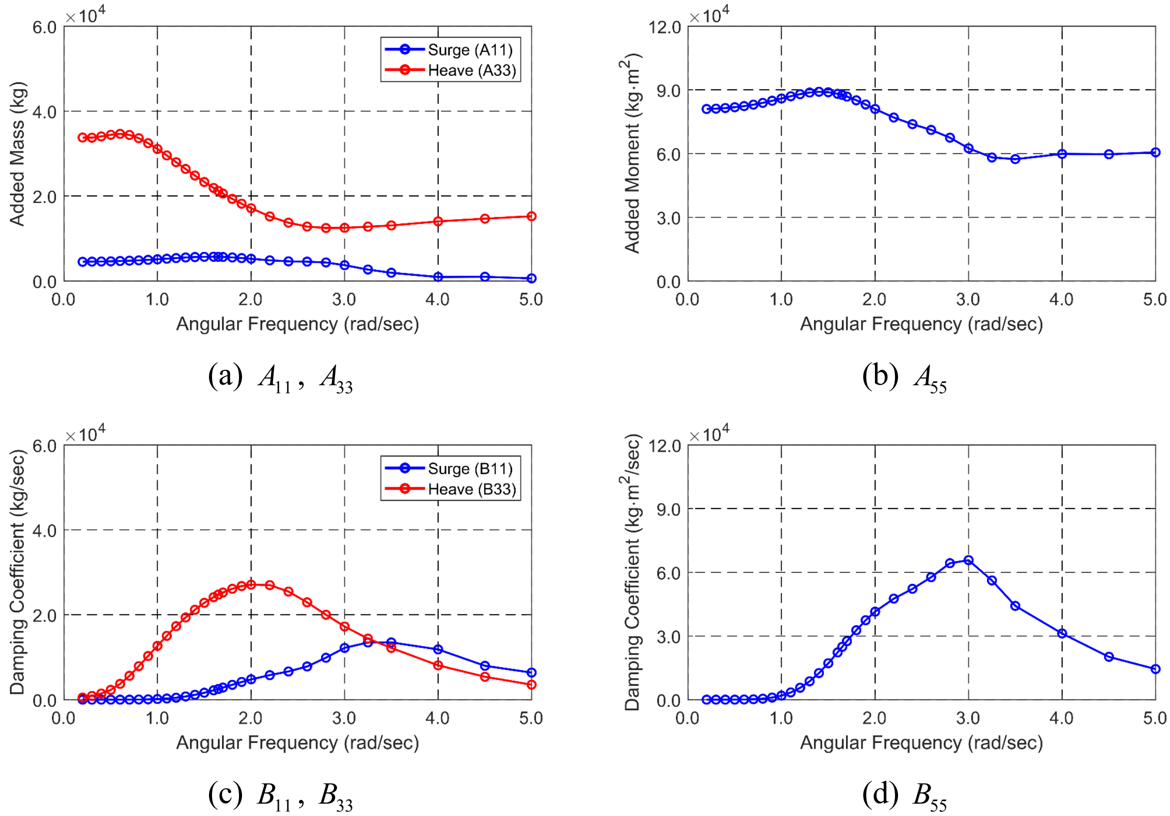

(a) A_{11}, A_{33} (b) A_{55}

(c) B_{11}, B_{33} (d) B_{55}

Fig. 12. Surge-heave-pitch added mass (a-b) and radiation damping (c-d) coefficients.

5.2. Time-Domain Simulation

The floater-mooring-LEG coupled dynamics simulations were performed in time domain for the performance estimation of SR-WEC. First, the LEG model was established through the initial parametric study with variable magnitudes of EMF and load resistance. A single-phase winding was employed in this study. Other generator parameters were the same as the parameters given in Prudell et al. [10]. Second, the magnet assembly's travel length, the coefficient of restitution at both ends, and the mass of the magnet assembly were selected for enhancing SR-WEC's performance. After each stage, the selected parameters were used as fixed parameters for the next parametric study. Last, the power-generation performance was quantitatively evaluated with the selected parameters under various random-wave excitations.

The time-domain model accounts for the viscous drag force on the outer cylinder. For the translational motions, the Morison equation was utilized with a drag coefficient of 0.5 acting at the outer cylinder's center of gravity, taking advantage of reference value in the experimental study at the representative surface roughness and Reynolds number [39]. For the rotational motions, a viscous damping ratio of 3% was assumed and inputted to the external damping matrix B_{ij}^{E} . The time step in the time-domain simulation was 0.005 sec to accommodate the generator dynamics accurately.

5.2.1. Environmental Condition

The JONSWAP wave spectrum was used for generating the time history of random waves. The range of significant wave heights was from 1 to 3.5 m while that of peak periods was from 4 to 11 sec. The time history of wave elevations was generated by the superposition of 100 regular waves, and signal repetition was prevented by the adoption of randomly perturbed frequency intervals. The total simulation time for each case was 1200 seconds, for which the ramping time of 300 seconds was not included in the statistical assessment. The enhancement parameter γ in the JONSWAP wave spectrum was estimated by the proposed equation in Ref [40]:

$$\begin{aligned} &\gamma = 5, && \text{on} \quad T_P / \sqrt{H_S} \le 3.6 \\ &\gamma = \exp\left(5.75 - 1.15 T_P / \sqrt{H_S}\right), && \text{on} \quad 3.6 < T_P / \sqrt{H_S} < 5 \\ &\gamma = 1, && \text{on} \quad 5 \le T_P / \sqrt{H_S} \end{aligned} \tag{22}$$

5.2.2. Parametric Study 1: Magnitudes of EMF and Load Resistance

Magnitudes of EMF (or magnitudes of PTO force i.e. term $B_f l_c$) and load resistance were first considered to design the PTO system. The PTO force acting on both the magnet and armature assemblies is a function of the induced current as given in Eq. (14), and the induced current is also related to the magnitudes of EMF, phase and load resistances, and phase inductance. Then, it is important to observe the relationship between these parameters and output power. In other words, the proper selection of these parameters can provide excellent sliding performance and output power simultaneously. Considering that EMF is a function of the relative velocity and the relative velocity also results from the PTO force, which is induced by the load resistance, the following parametric study can help in clarifying the role of LEG parameters to find improved output power.

In this parametric study, load resistance and the magnitude of EMF were in the range of 10 Ω to 200 Ω (10 Ω interval) and 100 T·m to 500 T·m (100 T·m interval), respectively. During the parametric studies, 3 wave conditions were selected, as summarized in Table 5. The sliding length, the coefficient of restitution, and the mass of the magnet assembly were fixed at 3 m, 0.38 (i.e., obtained in the actuator test), and 400 kg, respectively.

Table 5. Wave conditions for parametric studies.

H_S (m)	T_P (sec)	γ	Mean wave slope (deg)
1.0	5.0	1.0	6.4
2.0	6.0	2.4	7.2
3.0	7.0	3.0	7.5

Fig. 13 shows the time histories of displacement and velocity of the magnet assembly in the sliding direction, EMF, induced current, output power, and pitch motion of the outer cylinder at various load resistances and for *Hs*=2m. In Fig. 13, we show the simulation results for three representative load resistances of 20, 50, and 80 Ω to explain results better with time histories while the magnitude of EMF was set to 300 T·m. The sliding performance varies with different load resistances, as shown in Fig. 13(a-b). Both sliding displacements and velocities increase with the increasing load resistance. The trend of EMF is similar to that of relative velocity i.e. larger EMF at larger load resistance, as shown in Fig. 13(c). However, the current is inversely proportional to load resistance, as represented in Fig. 13(d). The smallest induced current in the circuit contributes to the reduction of the PTO force. As a result, the highest output power is acquired at the load resistance of 80 Ω, as shown in Fig. 13(e). Time histories for other load-resistance cases over 80 Ω were also checked. The results show that even if the sliding performance is better, the higher output power is not observed owing to a large reduction in the current that is a source of output power. Moreover, it is confirmed that the motion of the magnet assembly is highly influenced by the pitch motion of the outer cylinder when Fig. 13(a-b) is compared with Fig. 13(f). In comparison between Fig. 13 (a) and (e), it turns out that the given design has significant power generation when the reaction velocity occurs from the collision.

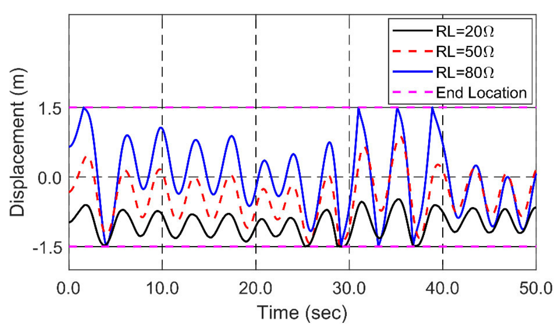

(a)

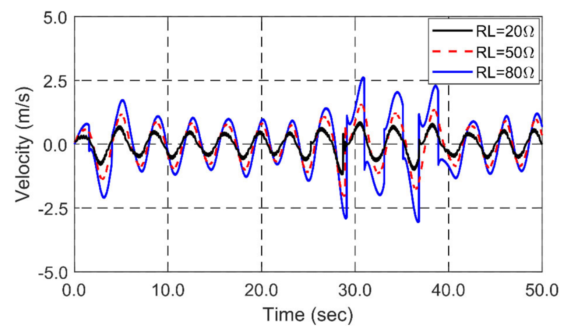

(b)

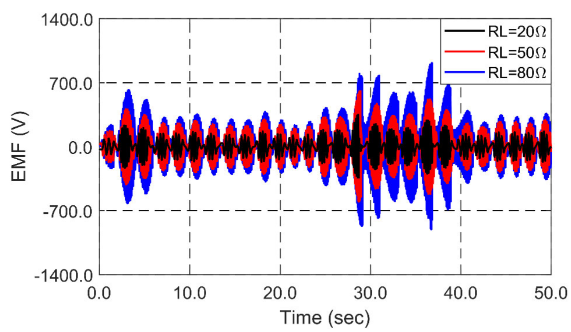

(c)

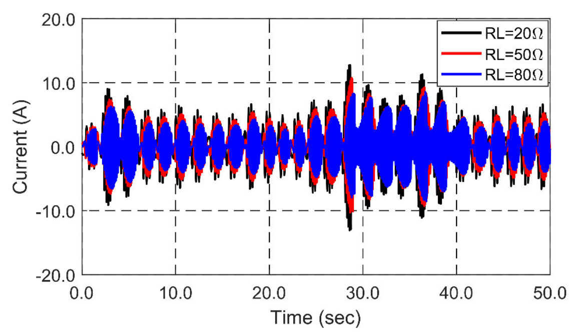

(d)

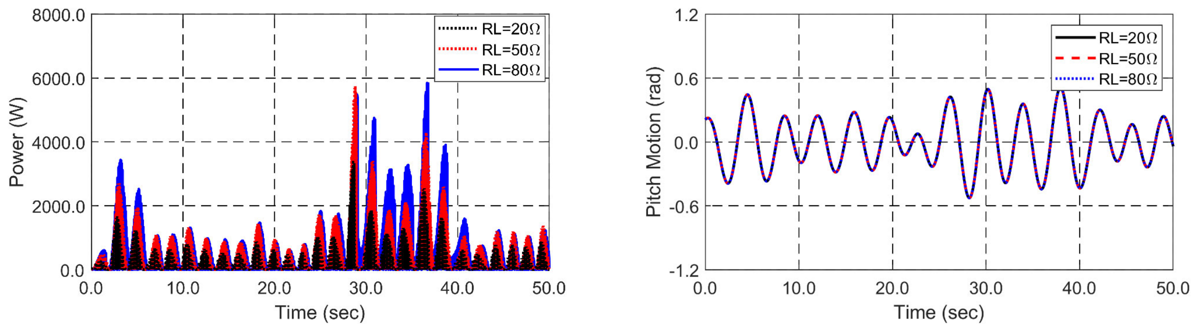

(e) (f)

Fig. 13. Time histories of displacement (a) and velocity (b) of the magnet assembly, EMF (c), induced current (d), output power (e), and pitch motion of outer cylinder (f) at different load resistances (H_S=2 m, T_P=6 sec).

Fig. 14 shows the average output power and load resistance at different magnitudes of EMF and wave conditions. The average output power is obtained from the time histories measured for 900 s. The observed load resistance with the highest output power at each magnitude of EMF is the same regardless of wave conditions. The larger the magnitude of EMF, the higher the load resistance. Besides, when the magnitude of EMF is higher than 300 T·m, there is no change in output power as the magnitude of EMF increases, and this phenomenon is observed regardless of the sea state. The magnitude of EMF and load resistance that produce the maximum average output power are 300 T·m and 80 Ω, respectively. These selected LEG parameters were to be fixed for the next parametric study.

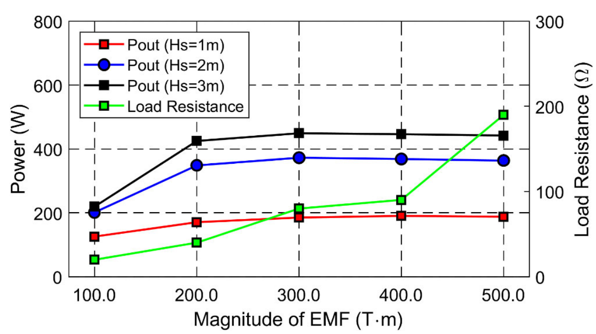

Fig. 14. Average output power and load resistance providing the maximum average output power at different magnitudes of EMF and wave conditions.

5.2.3. Parametric Study 2: Travel Length

The travel length of the magnet assembly, defined as the length between two ends minus the length of the magnet assembly, can improve the sliding performance. Various lengths of 2 m to 6 m were selected with 1-m interval and the proper length was evaluated. The coil is installed at the full length. Fig. 15 shows the time histories of displacement and velocity of the magnet assembly in the sliding direction, output power, and pitch motion of the outer cylinder at the different travel lengths. The magnet assembly can slide until it reaches both ends. In Fig. 15(a-b), interestingly, the magnet displacements and velocities become maximum when the travel length is 4 m. When the travel length is 2 m, the magnet assembly has to stop before it reaches the potentially maximum velocity. When the travel length is 6 m, the magnet does not slide the full length under the given wave condition as in Fig.15, so there is no improvement in output power. The magnet assembly gradually stops due to its inertial forces even after the pitch motion of the outer cylinder is switched in another direction. In this case, it can miss the best moment to slide in the other direction. Therefore, for the given wave conditions, the travel length at which average power becomes the highest is 4 m, as presented in Fig. 15(c). Moreover, the timely collisions at the ends are beneficial in increasing magnet sliding velocity, as in the case of travel lengths of 2 m and 4 m. Furthermore, significant variations between cases are observed after contacts at both ends occur under the large pitch motion of the outer cylinder (780-800 sec). When there is no contact under the small pitch motion (755-780 sec), there is a minor difference in velocity since other parameters and the pitch motions are the same among them.

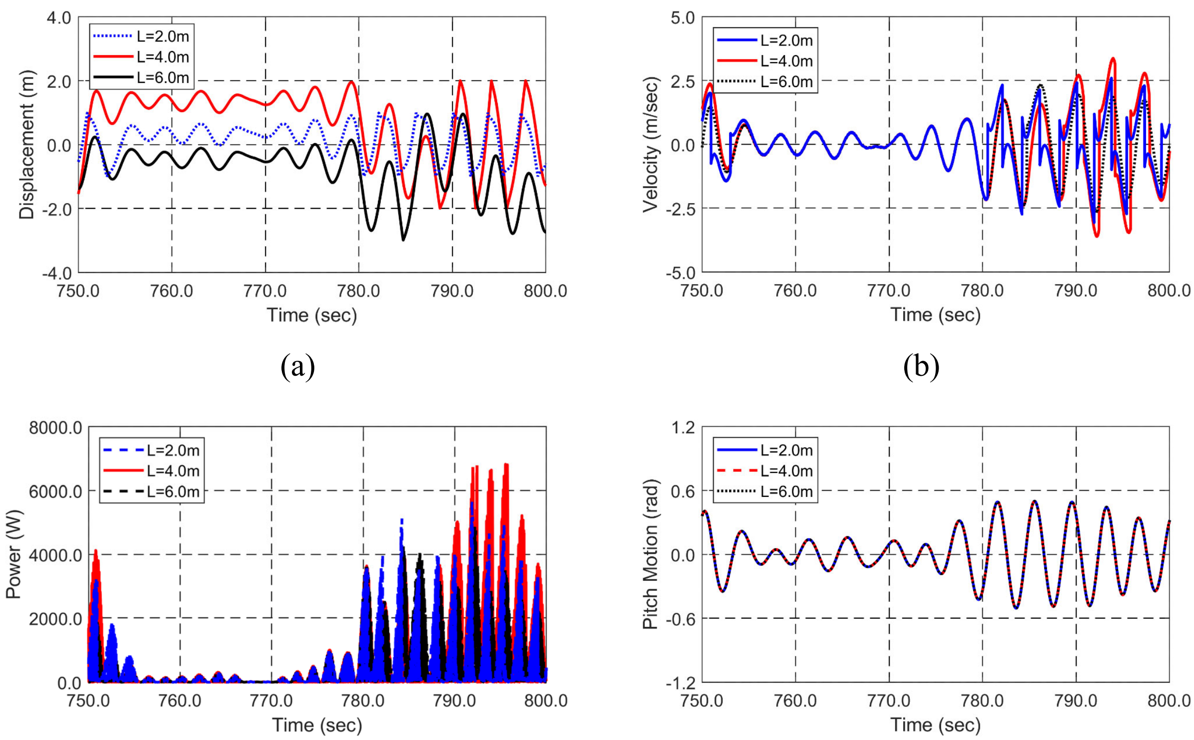

Fig. 15. Time histories of displacement (a) and velocity (b) of the magnet assembly, output power (c), and pitch motion of outer cylinder (d) at different travel lengths (H_S=2 m, T_P=6 sec).

Fig. 16 presents average output powers at different travel lengths and wave conditions. In the case of H_S=2 m (T_P=6 sec) and H_S=3 m (T_P=7 sec), the output power does not increase even though the travel length is increased beyond 4 m; instead, the output power rather starts to decrease after travel length=4 m. Therefore, travel length=4 m can be considered as the appropriate travel length after averaging the output powers of the 3 sea states. The case is also benefited by timely end collision. Higher significant wave heights generate greater pitch motions, which increases the sliding performance and output power. However, when the pitch motion is much larger than that of current environmental conditions, the design with the travel length of 6 m may be able to generate higher output power, which is discussed in Section 5.2.6. If the travel length is too short, the magnet assembly quickly reaches one end and remains almost stationary until it slides in the other direction. So, the corresponding power-generation efficiency becomes relatively low. The travel length was fixed to be 4 m for the next parametric study.

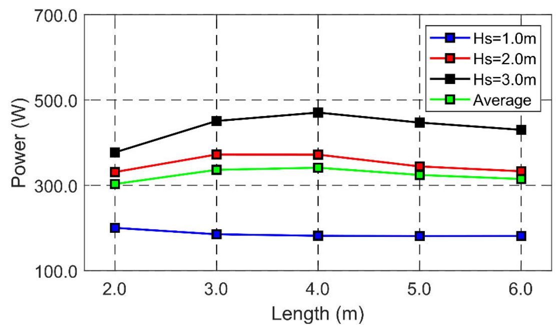

Fig. 16. Average output power at different travel lengths and wave conditions.

5.2.4. Parametric Study 3: Coefficient of Restitution

It was found in the previous parametric study that the timely elastic collision at both ends (+2 m and -2 m) helps the magnet assembly to better slide with rebounding velocities. To confirm the improvement of the sliding performance due to the reactive velocity from the collision, we analyzed the effect of the coefficient of restitution on the average output power. In this regard, three restitution coefficients, 0.01, 0.38 (given by the actuator test), and 0.8 were considered.

Fig. 17 shows the time histories of displacement and velocity of the magnet assembly in the sliding direction, output power, and pitch motion of the outer cylinder with the three different coefficients of restitution. Again, we observe the contact-induced substantial variations under the different coefficients of restitution when there is a significant pitch motion of the outer cylinder (780-800 sec). There is no contact when pitch motion is small (i.e. 750-780 sec), which leads to a minor difference in the sliding velocities since other parameters and the pitch motions are the same among them. When the timely collisions happen at the last stage of Re=0.38 and 0.8 cases (780-800 sec), the sliding velocities are increased due to the beneficial rebounding velocities after collisions. The higher the coefficient of restitution, the better the sliding performance and higher output power. This implies that the sliding performance can further be enhanced by placing highly restitutive elastic springs at both ends. Fig. 18 presents the average output power at different coefficients of restitution and wave conditions, and the above trends can further be confirmed. For the following parametric study, the coefficient of restitution was to be fixed at 0.8.

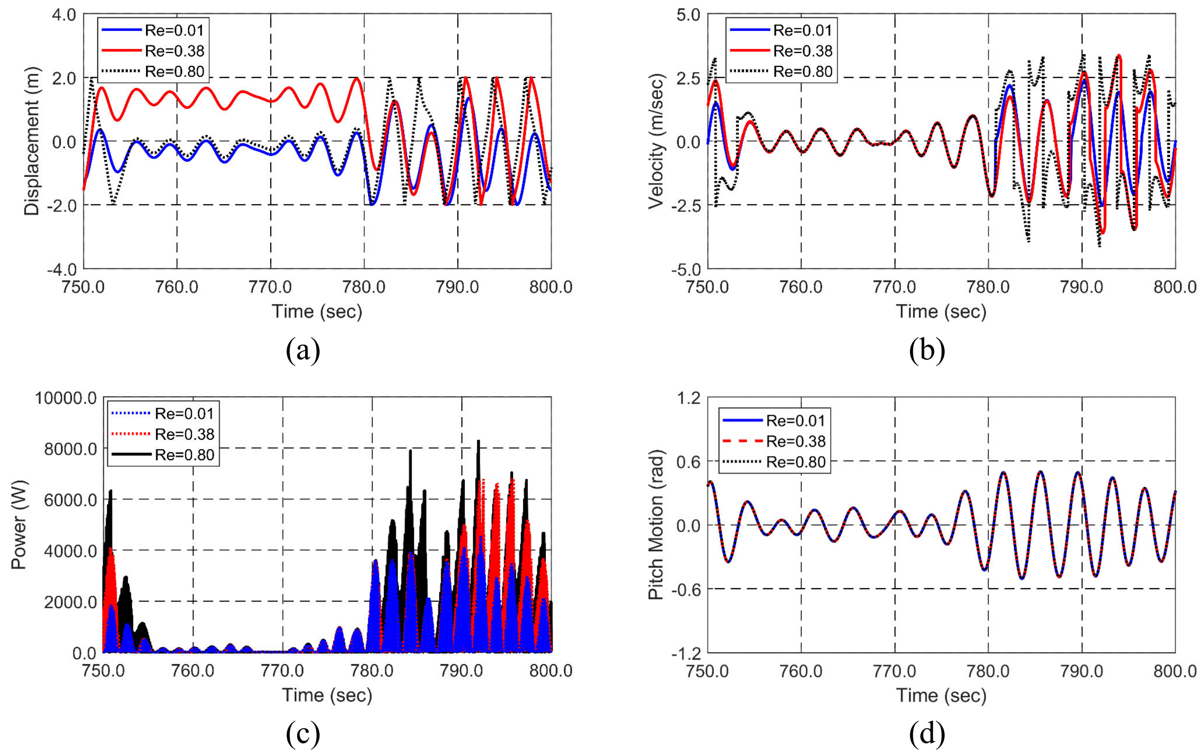

Fig. 17. Time histories of displacement (a) and velocity (b) of the magnet assembly, output power (c), and pitch motion of outer cylinder (d) at different coefficients of restitution (H_S=2 m, T_P=6 sec).

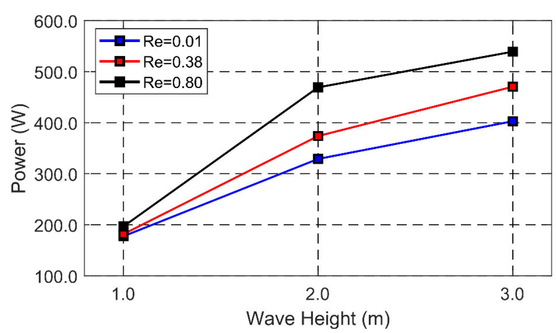

Fig. 18. Average output power at different coefficients of restitution and wave conditions.

5.2.5. Parametric Study 4: Mass of the Magnet Assembly

Since gravity is the primary source of power generation, the mass of the magnet assembly can significantly affect the sliding performance. In this regard, the magnet assembly's mass was varied in the simulations from 200 kg to 400 kg whereas the previous best parameters, including the coefficient of restitution of 0.8, were fixed. Fig. 19 shows the time histories of displacement and velocity of the magnet assembly in the sliding direction, output power, and pitch motion of the outer cylinder at different magnet masses. As shown in Fig. 19(a-c), the heavier the mass of the magnet assembly, the higher the sliding kinematics and output power. Moreover, significant variations among the cases are noticeably detected when contacts at both ends take place under the substantial pitch motion (180-200 sec). The average output power is presented in Fig. 20 for various magnet masses and sea states, and it also supports the previously mentioned trend. Thus, the mass of magnet assembly=400 kg was used in the previous simulations. Of course, much larger magnet mass beyond 400 kg will generate higher power but may cause larger structural impacts at both ends and also affect the pitch performance through the moment induced by the magnet mass and time-varying pitch mass moment of inertia. The center rod should also be strong enough to support a much larger magnet mass without bending.

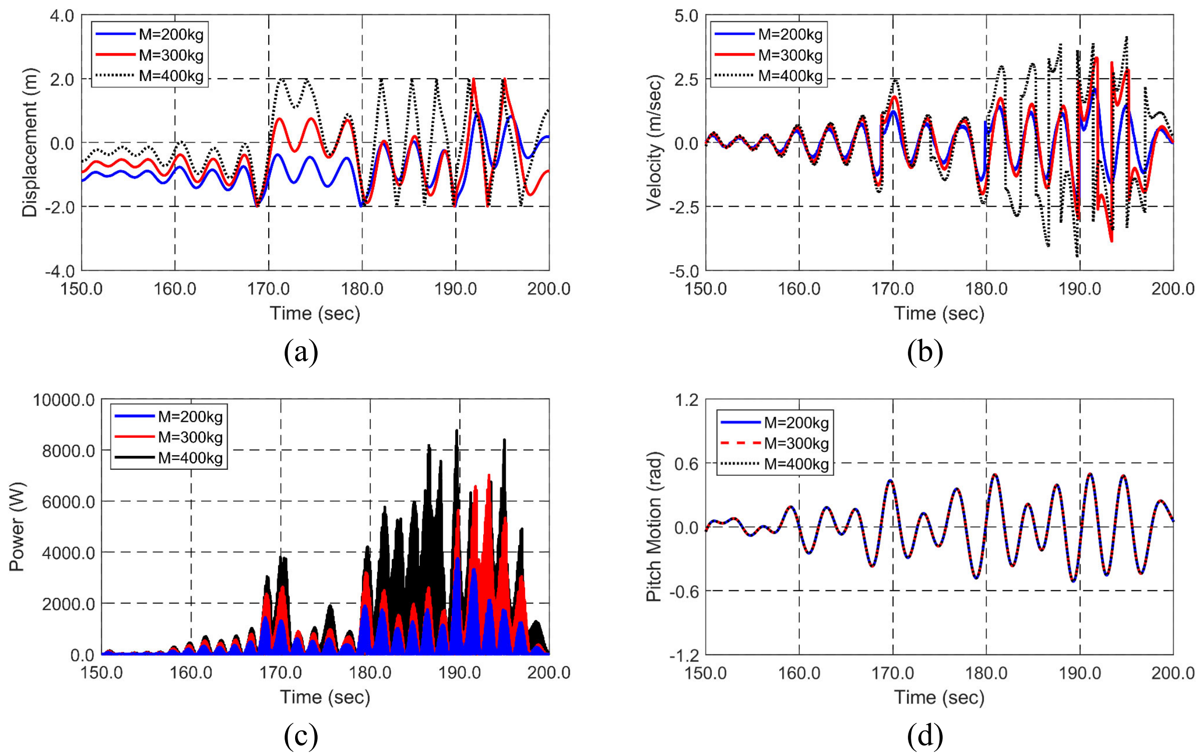

Fig. 19. Time histories of displacement (a) and velocity (b) of the magnet assembly, output power (c), and pitch motion of outer cylinder (d) at different masses of the magnet assembly (H_S=2 m, T_P=6 sec).

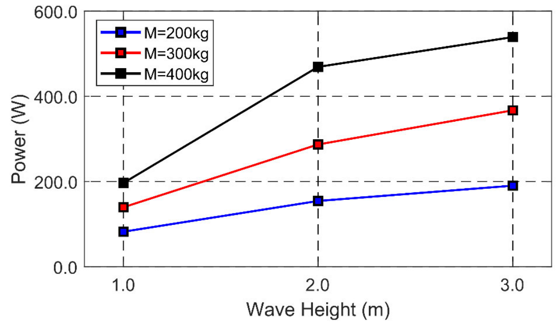

Fig. 20. Average output power at different masses of the magnet assembly and wave conditions.

5.2.6. Output-Power Calculations in Various Random Wave Conditions

The previous parametric studies demonstrate that adjustment of various system parameters can significantly improve the sliding performance and output power under 3 different wave conditions, as shown in Figs. 14, 16, 18, and 20. Much more time-domain simulations with enlarged random wave conditions were additionally performed to check the corresponding output power by using the parameters selected from the previous sections. The selected values of EMF magnitude, load resistance, travel length, coefficient of restitution, and magnet mass were 300 T·m, 80 Ω, 4 m, 0.8, and 400 kg, respectively, denoted as Case 1. As summarized in Table 6, we additionally simulated four more cases (Cases 2-5) to compare whether the chosen parameters can provide high output power.

Table 6. Case description.

Case number	EMF magnitude (T·m)	Load resistance (Ω)	Travel length (m)	Coefficient of restitution	Magnet mass (kg)
1	300	80	4	0.8	400
2	200	40	4	0.8	400
3	300	80	6	0.8	400
4	300	80	4	0.38	400
5	300	80	4	0.8	300

Fig. 21 shows the average output powers and RMS (root mean square) values of pitch motion of the outer cylinder at different significant wave heights from 1 m to 3.5 m and peak periods from 4 sec to 11 sec. Recall that the pitch natural frequency is 1.65 rad/s (3.81 sec). In this case, large pitch motions usually occur at low peak periods being closer to the pitch natural period, as shown in Fig. 21(f). Larger wave height also causes larger pitch motion under the identical peak period. Combining these two facts, it can be expected that the largest average output power occurs at the bottom-right corner of Fig.21(a-e) i.e. the lowest peak period and the highest wave height (H_S=3.5 m, T_P=4 sec). For Case 1, the corresponding average output power under the wave condition is 2.66 kW. However, even with H_S=3.5 m at T_P=11 sec (right-top corner), the average output power is only 0.13 kW. Therefore, the present SR-WEC is particularly designed to be efficient at low sea states, which is good since they cover more than 90% of typical annual sea states. In general, Case 1 shows the relatively high average output power compared with other cases. There are several environmental conditions where Case 2 has slightly higher output power than Case 1. Noticeably, in some conditions with the significant pitch motion at high wave height and low peak period, Case 3, in which travel length is 6 m, generates higher power than Case 1. For example, the maximum output power is 3.82 kW for Case 3 at H_S=3.5 m, T_P=4 sec. However, Case 1 still produces higher annual average power in that the occurrence of such wave condition is low. These comparisons support the parametric studies' role in finding a good combination of parameters to improve output power. The metaheuristic optimization algorithms such as the genetic algorithm and harmony search can be applied to optimize parameters to enhance output power further, and the results of the present parametric studies can be utilized to define the upper and lower boundaries of each parameter.

We calculated the capture width ratios for Case 1 with the average wave power and generated output power under random wave excitations [41], which are 9.3% at H_S = 1.5 m and T_P = 4 sec and 3.3% at H_S = 1 m and T_P = 5 sec.

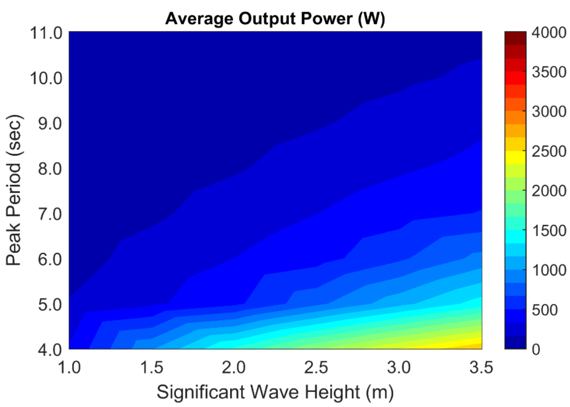

(a) Case 1

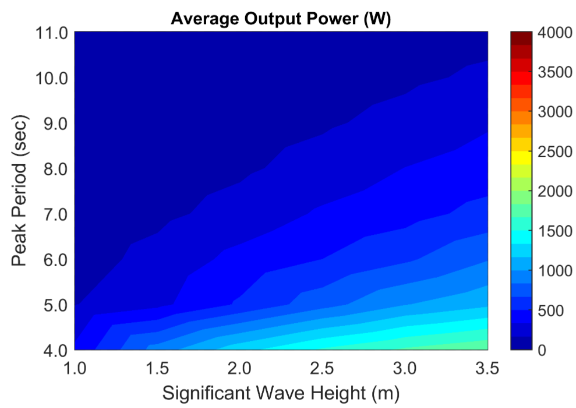

(b) Case 2

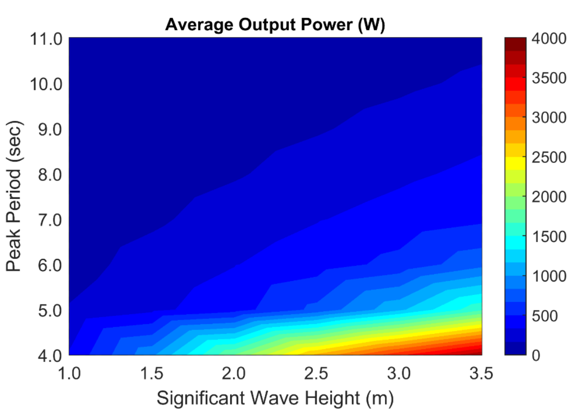

(c) Case 3

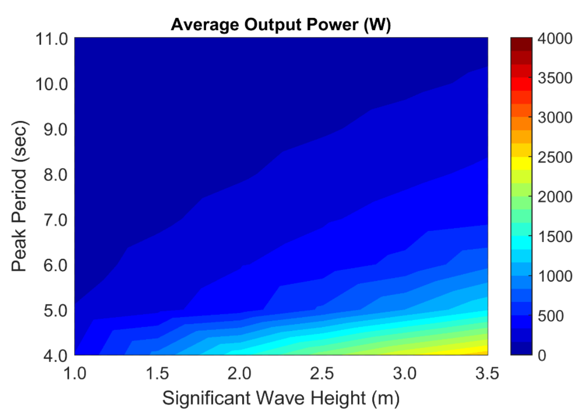

(d) Case 4

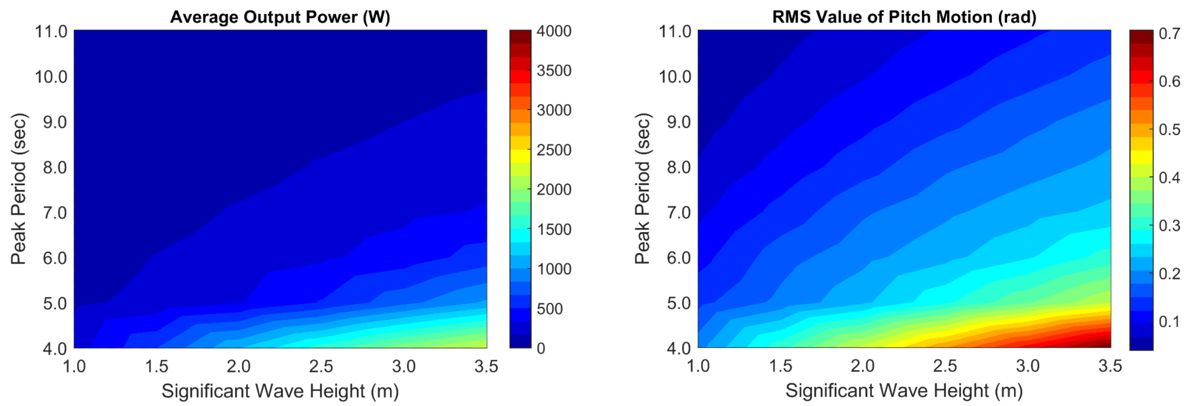

(e) Case 5 (f) Case 1

Fig. 21. Average output powers for Cases 1-5 (a-e) and RMS value of pitch motion of outer cylinder for Case 1 (f) under different random wave excitations.

Finally, we also checked the safety of the mooring line for various sea states, as presented in Fig. 22. In this case, studlink R4 chain was used, whose minimum breaking load (MBL) is 263.9 kN. When the safety factor of 1.67 is applied, as suggested by the API-mooring-design guideline, the allowable maximum mooring tension is 158 kN. In the present simulations, the maximum mooring tension is 126.7 kN in the case of H_S= 3.5 m and T_P= 4 sec, for which the largest outer-cylinder pitch motions and maximum power generation occur. It proves that the given mooring design is acceptable. In addition, the RMS value of mooring tension is large at high significant wave height and low peak period, similar to output power and pitch motion.

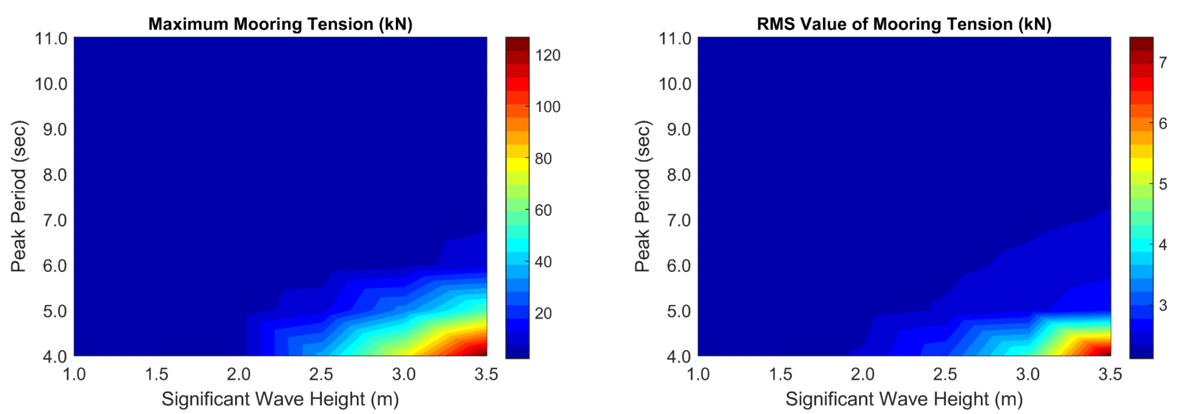

(a) (b)

Fig. 22. Maximum mooring tension (a) and RMS value (b) of mooring tension under different random wave excitations (Case 1).

6. Conclusions

In this study, the performance of SR-WEC was evaluated by the floater-mooring-LEG coupled time-domain simulations. SR-WEC consists of two bodies: the outer cylinder with an armature assembly (body #1) and a magnet assembly (body #2) sliding inside. For SR-WEC, the sliding displacement and velocity are mainly caused by gravity acceleration and the outer cylinder's motions, and they lead to electrical power generation.

During the developing stage, the proposed simulation tool was verified step by step by comparisons with laboratory tests. First, the numerically simulated sliding displacement and velocity were compared with those of heave-pitch coupled actuator tests by authors, which shows a good match. Second, the present generator-dynamics numerical solver was verified by the LEG experiment of [10], and the overall comparison is also excellent.

After verifying the simulation program, a series of parametric studies were carried out under different random wave conditions to find the appropriate design with increased output power. The selected design parameters were the magnitude of EMF, load resistance, travel length, mass of the magnet assembly, and restitution coefficient of end dampers. The time histories of sliding displacement and velocity of the magnet assembly and output power show that the performance of SR-WEC depends appreciably on those design parameters. After setting all the optimized parameters, the average output power was evaluated under largely extended random-wave conditions. The best performance of the SR-WEC is observed when the wave peak period is close to its natural period with the highest wave height. The resulting peak average output power is 2.66 kW at H_S= 3.5 m and T_P=4 sec. By riding along the surface without much structural resistance, mooring and structural designs can have benefits.

The SR-WEC performance can further be improved with semi-active and/or active control systems, such as the movable ring-type masses adjusting pitch natural frequency, latching control, and PTO-force control, which will be the subject of next study.

Acknowledgment

This research is supported by a U.S. DOE EERE WPTO project, DE-EE0008630. This work is also supported by the National Research Foundation of Korea (NRF) grant funded by the Korea government (MSIT) (No. 2017R1A5A1014883).

References

[1] I. Kralova, J. Sjöblom, Biofuels–renewable energy sources: a review. Journal of Dispersion Science and Technology, Vol. 31, 409-425, 2010.

[2] B. Drew, A.R. Plummer, M.N. Sahinkaya. A review of wave energy converter technology. Sage Publications Sage UK: London, England; 2009.

[3] P. Gadonneix, F.B. de Castro, N.F. de Medeiros, R. Drouin, C. Jain, Y.D. Kim, et al., 2010 survey of energy resources. London: World Energy Council, Vol., 593, 2010.

[4] G. Mork, S. Barstow, A. Kabuth, M.T. Pontes, Assessing the global wave energy potential. ASME 2010 29th International conference on ocean, offshore and arctic engineering, 447-454, 2010.

[5] R. Henderson, Design, simulation, and testing of a novel hydraulic power take-off system for the Pelamis wave energy converter. Renewable energy, Vol. 31, 271-283, 2006.

[6] J.P. Kofoed, P. Frigaard, E. Friis-Madsen, H.C. Sørensen, Prototype testing of the wave energy converter wave dragon. Renewable energy, Vol. 31, 181-189, 2006.
[7] K. Edwards, M. Mekhiche. Ocean power technologies powerbuoy®: system-level design, development and validation methodology. Proceedings of the 2nd Marine Energy Technology Symposium, METS2014. Seattle, WA; 2014. p. 1-9.
[8] A. Babarit, J. Hals, A. Kurniawan, M. Muliawan, T. Moan, J. Krokstad, The NumWEC project, Numerical estimation of energy delivery from a selection of wave energy converters. Final report, Starkraft, Centrale Nantes, NTNU, 1-317, 2011.
[9] N. Baker, M.A. Mueller. Direct drive wave energy converters. Rev Energ Ren: Power Engineering; 2001. p. 1-7.
[10] J. Prudell, M. Stoddard, E. Amon, T.K. Brekken, A. Von Jouanne, A permanent-magnet tubular linear generator for ocean wave energy conversion. IEEE Transactions on Industry Applications, Vol. 46, 2392-2400, 2010.
[11] J. Kim, H. Koh, I. Cho, M. Kim, H. Kweon, Experimental study of wave energy extraction by a dual-buoy heaving system. International Journal of Naval Architecture and Ocean Engineering, Vol. 9, 25-34, 2017.
[12] C. Jin, H. Kang, M. Kim, I. Cho, Performance estimation of resonance-enhanced dual-buoy wave energy converter using coupled time-domain simulation. Renewable Energy, Vol. 160, 1445-1457, 2020.
[13] E. Lejerskog, C. Boström, L. Hai, R. Waters, M. Leijon, Experimental results on power absorption from a wave energy converter at the Lysekil wave energy research site. Renewable energy, Vol. 77, 9-14, 2015.
[14] M. Stelzer, R. Joshi, Evaluation of wave energy generation from buoy heave response based on linear generator concepts. Journal of Renewable and Sustainable Energy, Vol. 4, 063137, 2012.
[15] S. Zheng, Y. Zhang, G. Iglesias, Concept and performance of a novel wave energy converter: Variable Aperture Point-Absorber (VAPA). Renewable Energy, Vol. 153, 681-700, 2020.
[16] X. Ji, E. Al Shami, J. Monty, X. Wang, Modelling of linear and non-linear two-body wave energy converters under regular and irregular wave conditions. Renewable Energy, Vol. 147, 487-501, 2020.
[17] B.W. Schubert, W.S. Robertson, B.S. Cazzolato, M.H. Ghayesh, Linear and nonlinear hydrodynamic models for dynamics of a submerged point absorber wave energy converter. Ocean Engineering, Vol. 197, 106828, 2020.
[18] Y. Hong, M. Eriksson, C. Boström, R. Waters, Impact of generator stroke length on energy production for a direct drive wave energy converter. Energies, Vol. 9, 730, 2016.
[19] A. Amiri, R. Panahi, S. Radfar, Parametric study of two-body floating-point wave absorber. Journal of marine science and application, Vol. 15, 41-49, 2016.
[20] S.-S. Park, S.M. Park, J. Jung, J.H. Kim, Analysis and experiments of the linear electrical generator in wave energy farm utilizing resonance power buoy system. Journal of Magnetics, Vol. 18, 250-254, 2013.
[21] Y. Gao, S. Shao, H. Zou, M. Tang, H. Xu, C. Tian, A fully floating system for a wave energy converter with direct-driven linear generator. Energy, Vol. 95, 99-109, 2016.
[22] J. Engström, V. Kurupath, J. Isberg, M. Leijon, A resonant two body system for a point absorbing wave energy converter with direct-driven linear generator. Journal of applied physics, Vol. 110, 124904, 2011.

[23] R. Haraguchi, T. Asai, Enhanced power absorption of a point absorber wave energy converter using a tuned inertial mass. Energy, Vol. 202, 117740, 2020.
[24] J. Kim, I.-H. Cho, M.-H. Kim, Numerical calculation and experiment of a heaving-buoy wave energy converter with a latching control. Ocean Systems Engineering, Vol. 9, 1-19, 2019.
[25] D. Son, R.W. Yeung, Optimizing ocean-wave energy extraction of a dual coaxial-cylinder WEC using nonlinear model predictive control. Applied Energy, Vol. 187, 746-757, 2017.
[26] H. Kang, M. Kim. Method and apparatus for wave energy conversion. Google Patents; 2019.
[27] N. Blažauskas, A. Pašilis, A. Knolis, Potential applications for small scale wave energy installations. Renewable and sustainable energy reviews, Vol. 49, 297-305, 2015.
[28] C.-H. Lee. WAMIT theory manual: Massachusetts Institute of Technology, Department of Ocean Engineering; 1995.
[29] W. Cummins. The impulse response function and ship motions. David Taylor Model Basin Washington DC; 1962.
[30] J. Morison, J. Johnson, S. Schaaf, The force exerted by surface waves on piles. Journal of Petroleum Technology, Vol. 2, 149-154, 1950.
[31] O. Faltinsen. Sea loads on ships and offshore structures. London, UK: Cambridge university press; 1993.
[32] D. Garrett, Dynamic analysis of slender rods. Journal of Energy Resources Technology, Vol. 104, 302-306, 1982.
[33] M. Kim, B. Koo, R. Mercier, E. Ward, Vessel/mooring/riser coupled dynamic analysis of a turret-moored FPSO compared with OTRC experiment. Ocean Engineering, Vol. 32, 1780-1802, 2005.
[34] C. Jin, M.-H. Kim, Tunnel-mooring-train coupled dynamic analysis for submerged floating tunnel under wave excitations. Applied Ocean Research, Vol. 94, 102008, 2020.
[35] Z. Ran, Coupled dynamic analysis of floating structures in waves and currents. PhD Dissertation Submitted to Texas A&M University, Vol., 2000.
[36] Z. Ran, M. Kim, W. Zheng, Coupled dynamic analysis of a moored spar in random waves and currents (time-domain versus frequency-domain analysis). Journal of Offshore Mechanics and Arctic Engineering, Vol. 121, 194-200, 1999.
[37] K. Rhinefrank, E. Agamloh, A. von Jouanne, A. Wallace, J. Prudell, K. Kimble, et al., Novel ocean energy permanent magnet linear generator buoy. Renewable Energy, Vol. 31, 1279-1298, 2006.
[38] C. Jin, M.-H. Kim, H. Kang, Time-Domain Simulations of the Coupled Dynamics of Surface Riding Wave energy converters. International Journal of Energy and Power Engineering, Vol. 13, 445-448, 2019.
[39] N. Thompson, Mean forces, pressure and flow field velocities for circular cylindrical structures: single cylinder with two-dimensional flow. EDU Data Item, Vol. 80025, 1980.
[40] N. Veritas. Environmental conditions and environmental loads: Det Norske Veritas; 2000.
[41] A. Babarit, A database of capture width ratio of wave energy converters. Renewable Energy, Vol. 80, 610-628, 2015.